Chemical
Science

ROYAL SOCIETY
OF CHEMISTRY

EDGE ARTICLE

View Article Online
View Journal | View Issue

Check for updates

Cite this: *Chem. Sci.*, 2022, **13**, 10824

All publication charges for this article have been paid for by the Royal Society of Chemistry

Excimer evolution hampers symmetry-broken charge-separated states†

Ebin Sebastian,‡ Jeswin Sunny‡ and Mahesh Hariharan*

Achieving long-lived symmetry-broken charge-separated states in chromophoric assemblies is quintessential for enhanced performance of artificial photosynthetic mimics. However, the occurrence of energy trap states hinders exciton and charge transport across photovoltaic devices, diminishing power conversion efficiency. Herein, we demonstrate unprecedented excimer formation in the relaxed excited-state geometry of bichromophoric systems impeding the lifetime of symmetry-broken charge-separated states. Core-annulated perylenediimide dimers (**SC-SPDI$_2$** and **SC-NPDI$_2$**) prefer a near-orthogonal arrangement in the ground state and a π-stacked foldamer structure in the excited state. The prospect of an excimer-like state in the foldameric arrangement of **SC-SPDI$_2$** and **SC-NPDI$_2$** has been rationalized by fragment-based excited state analysis and temperature-dependent photoluminescence measurements. Effective electronic coupling matrix elements in the Franck–Condon geometry of **SC-SPDI$_2$** and **SC-NPDI$_2$** facilitate solvation-assisted ultrafast symmetry-breaking charge-separation (SB-CS) in a high dielectric environment, in contrast to unrelaxed excimer formation (Ex*) in a low dielectric environment. Subsequently, the SB-CS state dissociates into an undesired relaxed excimer state (Ex) due to configuration mixing of a Frenkel exciton (FE) and charge-separated state in the foldamer structure, downgrading the efficacy of the charge-separated state. The decay rate constant of the FE to SB-CS ($k_{\mathrm{FE}\rightarrow\mathrm{SB-CS}}$) in polar solvents is 8–17 fold faster than that of direct Ex* formation ($k_{\mathrm{FE}\rightarrow\mathrm{Ex^*}}$) in non-polar solvent ($k_{\mathrm{FE}\rightarrow\mathrm{SB-CS}} \gg k_{\mathrm{FE}\rightarrow\mathrm{Ex^*}}$), characterized by femtosecond transient absorption (fsTA) spectroscopy. The present investigation establishes the impact of detrimental excimer formation on the persistence of the SB-CS state in chromophoric dimers and offers the requisite of conformational rigidity as one of the potential design principles for developing advanced molecular photovoltaics.

Received 6th August 2022
Accepted 18th August 2022

DOI: 10.1039/d2sc04387d

rsc.li/chemical-science

Introduction

Symmetry-breaking charge separation (SB-CS) is a photoexcited-state process by which a pair of identical chromophores forms a charge-separated state with the electron and hole localized on different chromophoric units.[1–7] Since discovering their existence in photosynthetic reaction centers, SB-CS processes have received tremendous attention.[8–13] Accomplishing SB-CS in a multichromophoric system is analogous to radical pair formation in silicon semiconductors, where exciton binding energy between a hole and an electron is overcome by thermal energy in silicon semiconductors.[3] The fundamental understanding of structure–property correlation and related excited-state dynamics among the molecular architectures has enabled researchers to rationalize the design of organic photovoltaics (OPVs).[14–18] Conventional donor–acceptor based OPVs generally exhibit low open-circuit voltages (V_{OC}) due to the significant energy difference between the optical band gap and charge-separated state at the interface.[16,19,20] However, the energy loss during SB-CS is low compared to that during charge separation (CS) in donor–acceptor systems.[3,21] Moreover, SB-CS processes in solid-states, transition metal complexes, and polymers are a progressing topic of interest and have been widely explored in weakly coupled multichromophoric systems.[2–4,22–24] Developing robust organic materials exhibiting optimized SB-CS and recombination dynamics is hence pivotal for the advancement of organic photovoltaics.

The factors determining the excited-state dynamics of SB-CS in multichromophoric architectures are the relative spatial orientation, distance and strength of electronic interaction between the monomeric units and the surrounding dielectric environment.[3,25–30] Among the various weakly coupled chromophoric assemblies investigated for SB-CS, multichromophoric perylenediimide (PDI) architectures are widely explored due to their exciting optoelectronic properties.[3,24,27,31] Of several interesting PDI molecular constructs reported to date, the spiro-conjugated orthogonal arranged PDI dimer (**Sp-PDI$_2$**) reported by our group exhibited a prolonged SB-CS state ($k_{\mathrm{SB-CS}}/k_{\mathrm{CR}}$ =

School of Chemistry, Indian Institute of Science Education and Research Thiruvananthapuram, Maruthamala P.O., Vithura, Thiruvananthapuram, Kerala, 695551, India. E-mail: mahesh@iisertvm.ac.in

† Electronic supplementary information (ESI) available. See https://doi.org/10.1039/d2sc04387d

‡ E. S. and J. S. contributed equally.

2647 in acetonitrile).[32] Ultrafast SB-CS in PDI dimers was first experimentally demonstrated by Wasielewski and coworkers in cofacial and head-to-tail stacked PDI dimers.[33] Würthner, Kim and coworkers recognized excimer as an intermediate state to SB-CS in a cofacially arranged PDI dimer.[26] In excimer-mediated excited state processes, the proficiency of the desired state is limited by the intermediate parasitic excimer formation.[26,34] The superposition of Frenkel exciton and the charge-transfer states in a chromophoric assembly populates the excimer state, which is generally considered an exciton trap state that diminishes the efficacy of OPVs.[35–39] Structural flexibility in the form of rotational or translational degrees of freedom in multichromophoric systems profoundly affects the population of distinct excited states.[40,41] The interchromophoric torsional motion in a bianthryl system facilitates the transition from the local excited state to the SB-CS state in accordance with solvent polarity.[42,43] Planarization of chromophores in the excited state reported in flexible molecular systems opens up diversified excited state dynamics.[44,45] Hence controlling the conformational flexibility and the concomitant manifestation of undesired radiative and non-radiative deactivation pathways of the SB-CS state is vital for a long-lived CS state, thereby enhancing photovoltaic efficiency.[3,46] Core-annulated near-orthogonal arranged perylenediimide dimers have found extensive applications as non-fullerene acceptors in organic solar cells owing to their greater solubility, reduced aggregation and excimer formation.[47,48] Though vital for photovoltaic applications, the excited-state dynamics of heteroatom annulated PDI dimers remain elusive. Our continuous efforts to understand the excited-state dynamics of orthogonal/near-orthogonal arranged multichromophoric architectures motivated us to dwell in the realm of excited-state structural rearrangement and the associated deactivation pathways.[32,44,49–53] Herein, we showcase the transformation of an initially populated SB-CS state to a detrimental excimer state due to excited-state conformational changes. Near-orthogonal stacked **SC-SPDI$_2$** and **SC-NPDI$_2$** undergo ultrafast structural relaxation to a foldamer structure, leading to a direct population of the excimer state in toluene. However, ultrafast SB-CS is favored over excimer formation in a polar environment due to the effective electronic coupling in Franck–Condon geometry (FC) and the thermodynamic feasibility of charge separation. The initially populated SB-CS state decays to an excimer state as the chromophore rearranges to a foldamer structure due to torsional flexibility, which is in contrast with SB-CS being facilitated by the torsional motion in bianthryl systems. Rigidification of the near-orthogonal arranged dimers emerges as an ideal strategy for achieving a long-lived charge-separated state and diminishing the unwanted deactivation pathway.

Results and discussion

Synthesis, characterization and geometry optimizations

In this work, sulfur and nitrogen annulated perylenediimide dimers, **SC-SPDI$_2$** and **SC-NPDI$_2$**, respectively, were synthesized and characterized following the reported and modified procedures (Fig. 1 and Scheme S1†).[47,54,55] **SPDI** and **NPDI** are the monomer units of **SC-SPDI$_2$** and **SC-NPDI$_2$**, respectively. In **SC-SPDI$_2$** and **SC-NPDI$_2$**, the monomeric units are covalently connected *via* a carbon–carbon single bond in the bay region of the perylenediimide core. The ground-state optimized geometries of **SC-SPDI$_2$** and **SC-NPDI$_2$** in vacuum were found to have an edge-to-edge arrangement between the monomeric units with a dihedral angle (φ) of 86.5° in **SC-SPDI$_2$** and 83.6° in **SC-NPDI$_2$**

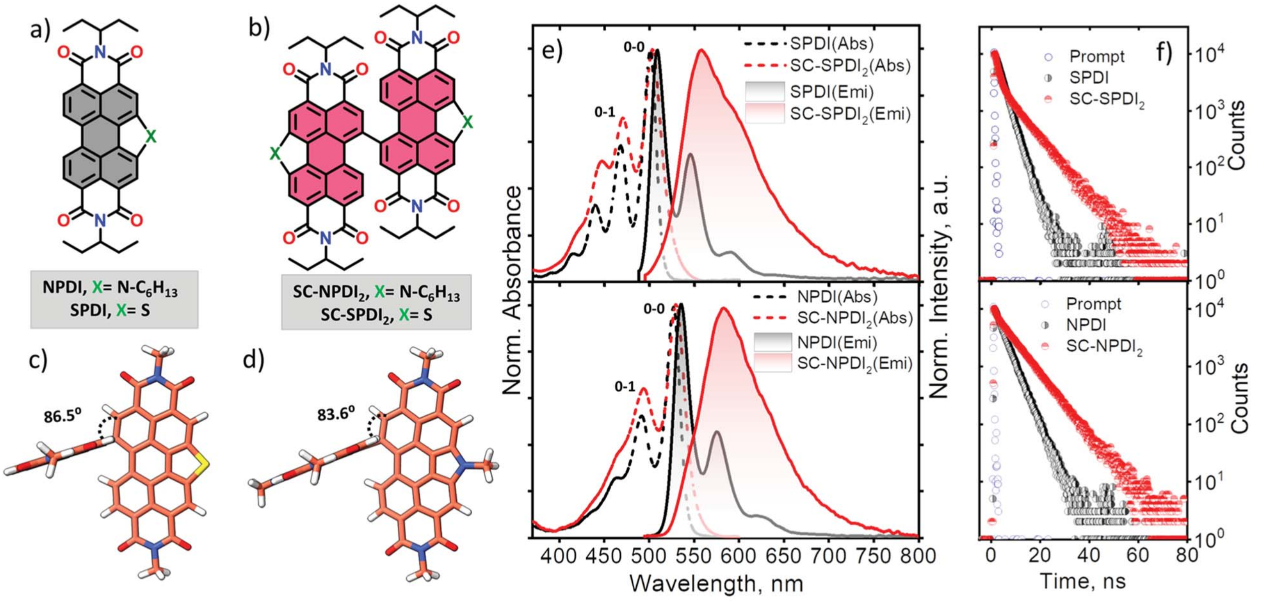

Fig. 1 Molecular structures of monomeric SPDI and NPDI (a) and dimeric SC-SPDI$_2$ and SC-NPDI$_2$ (b). Optimized geometries of SC-SPDI$_2$ (c) and SC-NPDI$_2$ (d) with the corresponding dihedral angles between the monomeric planes. Normalized UV-vis absorption and emission spectra (e) and fluorescence decay profile (f) of SC-SPDI$_2$ and SC-NPDI$_2$ in toluene at room temperature.

Table 1 Photoluminescence quantum yield (ϕ_{Fl}) and fluorescence lifetime (τ_{Fl}) of SPDI, NPDI, SC-SPDI$_2$, and SC-NPDI$_2$

	SPDI		**NPDI**		**SC-SPDI$_2$**		**SC-NPDI$_2$**	
Solvents	ϕ_{Fl}[a]	τ_{Fl} (ns)	ϕ_{Fl}[a]	τ_{Fl} (ns)	ϕ_{Fl}[a]	τ_{Fl} (ns)	ϕ_{Fl}[a]	τ_{Fl} (ns)
TOL ($\varepsilon = 2.38$)	0.58	2.73	0.68	3.34	0.60	1.42 (42), 8.35 (58)	0.71	0.84 (15), 7.86 (85)
ACE ($\varepsilon = 20.70$)	0.53	2.21	0.61	3.39	0.09	5.89	0.08	3.82
ACN ($\varepsilon = 37.50$)	0.55	2.15	0.62	3.31	0.08	5.81	<0.01	2.23

[a] Photoluminescence quantum yield (±5%).

(Fig. 1c and d). The single-crystal X-ray diffraction structure of **SC-NPDI$_2$** reported by Welch and coworkers exhibited a similar edge-to-edge arrangement with a dihedral angle of 66°, which is significantly lower than that observed in the optimized structure due to the crystal packing forces in the solid-state.[47] The incorporation of S and N atoms on the perylene core of PDI imposed a curved or bowed molecular geometry as a consequence of the ring strain of the fused heteroring (Fig. S1†).[56,57] The computed carbon-heteroatom bond lengths in the annulated heteroring of **SC-SPDI$_2$** and **SC-NPDI$_2$** indicate that the ring strain induced by the thiophene ring (C–S bond length: 1.77 Å, Fig. S2†) on the **PDI** core is weaker than that induced by the pyrrole ring (C–N bond length: 1.41 Å, Fig. S2†).

Optical properties

The steady-state electronic properties of **SC-SPDI$_2$** and **SC-NPDI$_2$** along with the monomeric units were explored by electronic absorption and photoluminescence spectroscopy measurements in toluene (TOL, $c_0 = 0.1$–0.3 μM) at room temperature (Fig. 1e). The UV-visible absorption spectrum of **NPDI** shows characteristic spectral signatures of perylenediimide (PDI) dye with an absorption maximum (λ_{max}^{Abs}) at 527 nm, while **SPDI** ($\lambda_{max}^{Abs} = 501$ nm) shows a 26 nm hypsochromic shift compared to PDI and **NPDI** (Fig. S3†). As a result of the near-orthogonal arrangement, **SC-SPDI$_2$** and **SC-NPDI$_2$** show negligible red-shifted electronic absorption spectra with absorption maxima centered at 503 and 530 nm (Tables S1–S4†).[32,58] The ratio of the intensity of the first and second vibronic bands, I_{0-0}/I_{0-1}, of **SC-SPDI$_2$** (1.42) and **SC-NPDI$_2$** (1.55) decreased from that of monomeric **SPDI** (1.70) and **NPDI** (1.92), indicating weak H-type excitonic coupling between the monomeric units (Fig. 1e).[59,60] In addition, the slight broadening of the 0–0 vibronic absorption band of **SC-SPDI$_2$** and **SC-NPDI$_2$** as compared to that of the monomeric unit reiterates the weak excitonic coupling in near-orthogonal dimers.

As shown in Fig. 1e, photoexcitation of **SPDI** and **NPDI** at 470 nm displays a characteristic PDI photoluminescence spectrum with an emission maximum (λ_{max}^{Em}) observed at 509 nm and 535 nm, respectively (Stokes shift of ~8 nm). The photoluminescence quantum yield (ϕ_{Fl}) of **SPDI** and **NPDI** is quantified as 0.58 and 0.68 in toluene, respectively (Table 1). Fascinatingly, **SC-SPDI$_2$** and **SC-NPDI$_2$** reveal a significantly red-shifted (Stokes shift of ~54 nm) and broadened photoluminescence spectrum relative to the monomeric **SPDI** and **NPDI** in TOL ($\lambda_{max}^{Em} = 558$ nm for **SC-SPDI$_2$** and 584 nm for **SC-NPDI$_2$**). Broad, featureless, and extensive Stokes shifted photoluminescence spectra are the characteristic spectral features of an excimer (Ex) state.[29,35,61,62] Ex states, an admixture of Frenkel exciton (FE) and charge transfer (CT) states, are generally considered as energy trap states with increased non-radiative decay rates.[27,54,55] However, the photoluminescence quantum yields of dimers are not drastically quenched, $\phi_{Fl} = 0.60$ for **SC-SPDI$_2$** and $\phi_{Fl} = 0.71$ for **SC-NPDI$_2$**, as compared to that of the reference molecules (**SPDI** and **NPDI**), suggesting an excimer-like state having a large FE contribution (*vide infra*, Table 1).[4,63,64]

To further scrutinize the nature of the emissive state of **SC-SPDI$_2$** and **SC-NPDI$_2$**, fluorescence lifetime measurements were performed in TOL. **SC-SPDI$_2$** and **SC-NPDI$_2$** exhibit biexponential decay of emission with lifetimes of ${\tau_{Fl}}^1 = 1.42$ ns and ${\tau_{Fl}}^2 = 8.15$ ns for **SC-SPDI$_2$** and ${\tau_{Fl}}^1 = 0.84$ ns and ${\tau_{Fl}}^2 = 7.86$ ns for **SC-NPDI$_2$** (Fig. 1f and Table 1), suggesting the presence of dual emissive states in the dimers. Monomeric **SPDI** and **NPDI** in TOL display a monoexponential decay profile with a lifetime of $\tau_{Fl} = 2.73$ ns and $\tau_{Fl} = 3.34$ ns, respectively. Since the fluorescence lifetime of the Ex state is reported to be longer than that of the monomer unit, the long-lived emissive component of **SC-SPDI$_2$** (${\tau_{Fl}}^2 = 8.15$ ns) and **SC-NPDI$_2$** (${\tau_{Fl}}^2 = 7.86$ ns) might stem from the Ex states.[26,35] The dual emissive nature of **SC-SPDI$_2$** and **SC-NPDI$_2$** indicates that the dimers in the FC geometry may undergo a structural change in the excited state and form a different state, possibly an unrelaxed excimer state (Ex*), which can emit photons before completely relaxing to the relaxed excimer state.[36,40,65] However, the most intriguing aspect of the emissive excited-state of **SC-SPDI$_2$** and **SC-NPDI$_2$** is that the population of Ex states does not quench photoluminescence quantum yield. What could be the excited-state structure that promotes the aforementioned optical properties? To address this, theoretical and experimental techniques have been employed to unravel the underlying excited-state phenomena.

Excited-state geometry optimizations

In order to obtain an in-depth insight into the excited-state relaxed structure, density functional theory-based geometry optimization has been performed in the excited-state by applying the dispersion corrected functional (TD-B3LYP-D3/def2-svp level of theory).[66–69] The theoretical calculations propose that the ground state (S_0) near-orthogonal arrangement of **SC-SPDI$_2$** and **SC-NPDI$_2$** gets transformed into the nearly π-stacked foldamer conformation in the excited state (S_1) (Fig. 2

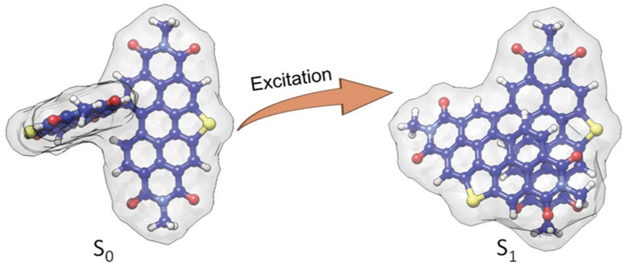

Fig. 2 Excited-state structural relaxation of SC-SPDI$_2$ dimer upon photoexcitation.

and S4†). Due to excited-state structural relaxation, the electronic interaction between the monomeric units increases as the dihedral angle (φ) between monomeric units decreases from 86.5° to 57.6° in **SC-SPDI$_2$** and from 83.6° to 62.5° in **SC-NPDI$_2$**. Furthermore, the centroid-to-centroid distance (d) between annulated PDIs decreases from 5.94 Å to 4.47 Å for **SC-SPDI$_2$** and 5.73 Å to 4.46 Å for **SC-NPDI$_2$** upon excited-state structural relaxation (Fig. S4†). Several bichromophores and multichromophores have also been identified to exhibit foldamer arrangements in distinct environments.[70–73] Schwartz and coworkers reported the existence of two conformers (near-orthogonal and nearly π-stacked arrangement) in the ground state of a non-annulated bay-linked perylenediimide dimer (di-PDI, Fig. S5†).[74] The absence of two minima in the ground state potential energy surfaces of **SC-SPDI$_2$** and **SC-NPDI$_2$** when the dihedral angle changes from 45° to 125°, in contrast to di-PDI, could be ascribed to the effect core-annulation has in altering the energy landscapes (Fig. S6†).

Time-resolved emission spectroscopy measurements

To obtain deep insights into the energy landscape of excited-state structural relaxation and excimer formation of **SC-SPDI$_2$** and **SC-NPDI$_2$** in TOL, we have performed picosecond time-resolved emission spectroscopy (TRES) measurements (pulse width <60 ps, Fig. S7 and S8,† ESI, Section 1.2†). The global analysis of TRES data of **SC-SPDI$_2$** and **SC-NPDI$_2$** using sequential model A → B indicate the presence of two dependent emissive states. Evolution associated spectra of the first species (EAS$_\mathrm{A}$) show an intense emission band that resembles the steady-state emission spectra of **SC-SPDI$_2$** with $\lambda_{\mathrm{max}}^{\mathrm{Em}}$ at 559 nm, which is assigned to the unrelaxed excimer (Ex*, Fig. S7 and S9†).[75] The Ex* state decays to a weakly emissive stable excimer state (Ex) with a time constant of $\tau_{\mathrm{Ex^*\rightarrow Ex}} = 1.37$ ns. Weakly emissive, broadened, and red-shifted ($\lambda_{\mathrm{max}}^{\mathrm{Em}} = 564$ nm) photoluminescence features are characteristics of an excimer state (EAS$_\mathrm{B}$) with a lifetime of 8.30 ns (Fig. S7†). Similarly, **SC-NPDI$_2$** in TOL exhibits emissive unrelaxed and relaxed excimer states (EAS$_\mathrm{A}$ and EAS$_\mathrm{B}$), which decay with time constants of 0.74 ns and 7.74 ns (Fig. S8 and S9†). The relaxed excimer state (Ex) observed is weakly emissive in nature with red-shifted ($\lambda_{\mathrm{max}}^{\mathrm{Em}} =$ 584 nm) and broader spectral properties than those of the strongly emissive unrelaxed excimer state ($\lambda_{\mathrm{max}}^{\mathrm{Em}} = 579$ nm). TRES measurement unambiguously confirms that the structural relaxation energetically stabilizes the excimer state and gradually reduces the photoluminescence properties.

Temperature-dependent photoluminescence measurements

Further insights into the excited-state structural relaxation of **SC-SPDI$_2$** and **SC-NPDI$_2$** dimers in TOL were provided by steady-state temperature-dependent photoluminescence (PL) measurements from 90 K to 250 K (Fig. 3).[75–77] Interestingly, at 90 K, **SC-SPDI$_2$** and **SC-NPDI$_2$** show PL spectra with well-resolved vibronic progression and a hypsochromic shifted emission maximum ($\lambda_{\mathrm{max}}^{\mathrm{Em}} = 540$ nm for **SC-SPDI$_2$** and $\lambda_{\mathrm{max}}^{\mathrm{Em}} =$ 557 nm **SC-NPDI$_2$**) as compared to the PL characteristics of dimers observed at room temperature (Fig. S10†). Moreover, the 0–0 transition approximately matches the corresponding absorption spectrum onset and is assigned to emission from

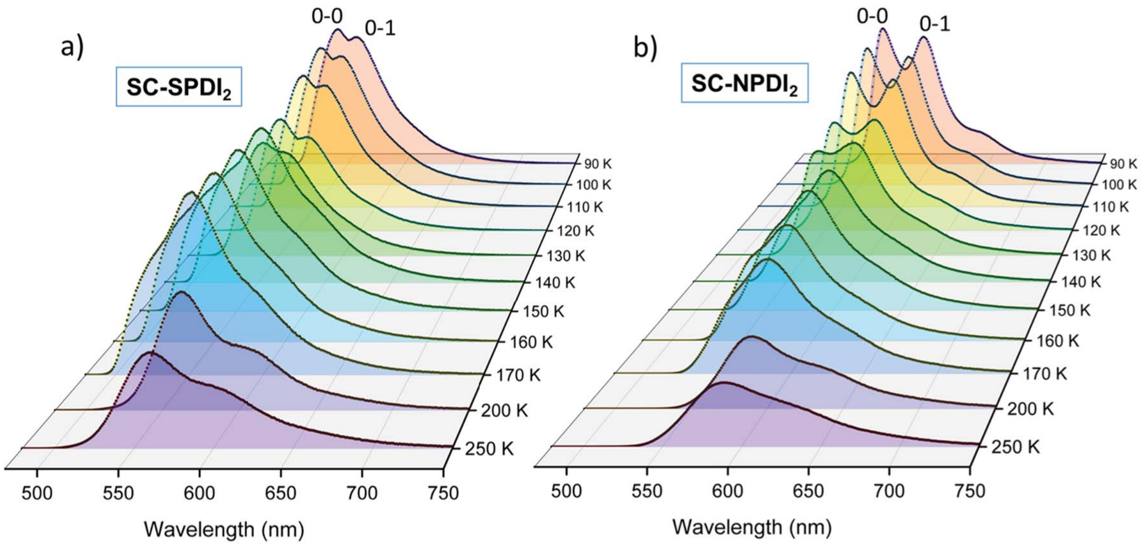

Fig. 3 The temperature-dependent photoluminescence spectra of (a) SC-SPDI$_2$ and (b) SC-NPDI$_2$ in toluene.

the Frenkel exciton (FE) state. The observed PL spectra of **SC-SPDI$_2$** and **SC-NPDI$_2$** at 90 K resemble emission features of a monomeric unit with a decrease in the 0–0 to 0–1 PL line strength ratio, which confirms the delocalization of excitation energy among both monomeric units in the Franck–Condon geometry (Fig. S11†).[78] As the temperature increases, a gradual reduction in the PL intensity and an inversion in the vibronic peak ratio are observed, indicating the transformation of FC geometry to an H-type foldamer conformation (Fig. 3).[79,80]

At the warming temperature of TOL between 140 K and 170 K, vibronically resolved PL features from the FE disappear and broader, less featured, and red-shifted PL spectra evolve ($\lambda_{\max}^{\mathrm{Em}}$ = 552 nm and 582 nm for **SC-SPDI$_2$** and **SC-NPDI$_2$**, respectively). The observed PL spectra (140 K–170 K) resemble the time-resolved emission spectral signatures of the unrelaxed excimer (Ex*) state and emission from the Ex* state is more predominant with an overlapping component of a minor amount of emission from the FE state (Fig. S12†). The PL intensity of **SC-SPDI$_2$** at warming temperature is slightly higher than that at 130 K, indicating the higher transition strength of the Ex* state than the FE state. At the same time, the PL intensity of **SC-NPDI$_2$** decreases gradually as the temperature increases from 90 K to 170 K. Finally, at high temperatures (>170 K), PL spectra are further broadened and red-shifted ($\lambda_{\max}^{\mathrm{Em}}$ = 560 and 587 nm for **SC-SPDI$_2$** and **SC-NPDI$_2$**, respectively) and PL intensity decreases dramatically, representing the formation of a relaxed excimer state (Ex), which resembles the room temperature PL spectra. The overlapping emissions of the unrelaxed excimer state (Ex*) and energy stabilized excimer state (Ex) define the PL emission spectra in this region (>170 K), and FE state emission is virtually absent, which could be due to the ultrafast structural reorganization (*vide infra*). The temperature-dependent PL measurement demonstrates the transformation of the FC geometry of **SC-SPDI$_2$** and **SC-NPDI$_2$** to a relaxed foldamer structure by excited-state structural relaxation at room temperature. Similarly, PL measurements of **SC-SPDI$_2$** and **SC-NPDI$_2$** in a polystyrene matrix support the near-orthogonal arrangement in the solid state (Fig. S13†).[81]

Solvent-dependent optical properties

To understand the surrounding dielectric environment moderated excited-state properties of **SC-SPDI$_2$** and **SC-NPDI$_2$**, we carried out absorption and fluorescence measurements in solvents of different dielectric constants, *i.e.*, toluene (TOL, ε = 2.38), acetone (ACE, ε = 20.70), and acetonitrile (ACN, ε = 37.50). The solvent-dependent UV-vis absorption spectra of **SC-SPDI$_2$** and **SC-NPDI$_2$** exhibit virtually unperturbed absorption line shapes, which is also the case for monomeric **SPDI** and **NPDI** (Fig. S14–S16† and Table 1). On the other hand, normalized solvent-dependent emission spectra of **SC-SPDI$_2$** and **SC-NPDI$_2$** show emission band broadening and a red-shift in the emission maximum as the polarity of the solvent increases from TOL to ACE (Fig. S17†). This solvent dependency of **SC-SPDI$_2$** and **SC-NPDI$_2$** implies the stabilization of the emissive excimer state as the solvent polarity increases. As the solvent polarity increases from ACE to ACN, **SC-NPDI$_2$** reflects gradual peak broadening and an increase in Stokes shifts in normalized emission spectra. This observation reveals the stronger charge-transfer character of the excimer state in **SC-NPDI$_2$**.[29,82] However, the normalized emission spectra of **SC-SPDI$_2$** exhibit minor changes as the polarity changes from ACE to ACN, indicating the weaker charge transfer characteristics of the excimer state of **SC-SPDI$_2$** in polar solvents.

The photoluminescence quantum yield (ϕ_{Fl}) of **SC-SPDI$_2$** and **SC-NPDI$_2$** drastically decreases with the increase in solvent polarity from TOL to ACE, presumably due to competitive non-radiative decay channels and the increased CT character of the excimer state (ϕ_{Fl} = 0.60 in TOL, 0.09 in ACE for **SC-SPDI$_2$** and ϕ_{Fl} = 0.71 in TOL, 0.08 in ACE for **SC-NPDI$_2$**, Table 1). **SC-NPDI$_2$** exhibits further quenching of photoluminescence as solvent polarity changes from ACE to ACN; in contrast, **SC-SPDI$_2$** exhibits negligible effects as the solvent polarity changes from ACE to ACN. The unique dielectric environment-dependent ϕ_{Fl} of **SC-SPDI$_2$** and **SC-NPDI$_2$** indicates the variation in the CT nature of the emissive excimer state as the solvent and molecular structure change (ϕ_{Fl} = 0.09 in ACE, 0.08 in ACN for **SC-SPDI$_2$** and ϕ_{Fl} = 0.08 in ACE, <0.01 in ACN for **SC-NPDI$_2$**).

The solvent-dependent fluorescence lifetime measurements of **SC-SPDI$_2$** and **SC-NPDI$_2$** show the disappearance of a shorter-lived fluorescence decay component and a decrease in the fluorescence lifetime of the second component as the solvent polarity increases from TOL to ACE (Table 1 and Fig. S18†). Additionally, as the dielectric medium changes from ACE to ACN, a negligible difference in the fluorescence lifetime was observed for **SC-SPDI$_2$** (τ_{Fl} = 5.89 ns in ACE and 5.81 ns in ACN). However, **SC-NPDI$_2$** displays a slight decrease in the fluorescence lifetime as the polarity of the solvent increases (τ_{Fl} = 3.82 ns in ACE and 2.23 ns in ACN; Table 1 and Fig. S18†). This discrepancy implies the dielectric dependency of the excimer state of **SC-NPDI$_2$**. The solvent-dependent photoluminescence quenching and decrease in the fluorescence lifetime of **SC-SPDI$_2$** and **SC-NPDI$_2$** in more polar solvents (ACE and ACN) implies the existence of an additional non-radiative deactivation channel such as SB-CS and an increase in the CT character of the excimer.[62] Photoluminescence quantum yield and fluorescence lifetimes of monomers **SPDI**/**NPDI** are nearly insensitive to solvent polarity (Fig. S19† and Table 1).

Energetics

In order to determine the feasibility of the photoinduced SB-CS in **SC-SPDI$_2$** and **SC-NPDI$_2$** in polar solvents, the

Table 2 Driving forces (ΔG), time constants (τ), and rate constants (k) for symmetry-breaking charge separation (SB-CS) of SC-SPDI$_2$ and SC-NPDI$_2$ in different solvents

	Solvents	ΔG_{CS} (eV)	τ_{CS} (ps)	$k_{\mathrm{CS}} \times 10^{11}$ (s^{-1})
SC-SPDI$_2$	TOL	+0.20	—	—
	ACE	−0.42	1.5 ± 0.3	6.67
	ACN	−0.46	0.9 ± 0.2	11.1
SC-NPDI$_2$	TOL	+0.25	—	—
	ACE	−0.40	2.7 ± 0.2	3.70
	ACN	−0.43	1.4 ± 0.1	7.14

thermodynamic driving force (ΔG_{CS}) for the SB-CS process has been analysed using the Weller formulation (Fig. S20,† Tables 2 and S9,† ESI, Section 1.4).[83] The Weller analysis gives $\Delta G_{SB-CS} \approx -0.42$ and -0.46 eV for **SC-SPDI$_2$** and $\Delta G_{SB-CS} \approx -0.40$ and -0.43 eV for **SC-NPDI$_2$** in ACE and ACN respectively, indicating that SB-CS is thermodynamically favored in ACE and ACN (exergonic process) as compared to non-polar TOL ($\Delta G_{SB-CS} \approx +0.20$ and $+0.25$ eV respectively, endergonic process).[84] The electronic interaction between the frontier molecular orbitals of the adjacent monomeric units in the FC geometry of **SC-SPDI$_2$** and **SC-NPDI$_2$** provides the required electronic coupling for charge separation (Fig. S21 and S22†).[3,32]

Excited-state population dynamics

To shed light on excited-state dynamics accountable for the excimer formation, solvent-dependent fluorescence quenching and SB-CS in **SC-SPDI$_2$** and **SC-NPDI$_2$**, femtosecond transient absorption (fsTA) measurements of the annulated PDI dimers were performed (ESI, Sections 1.5 and 1.6†). The solvent-dependent fsTA spectra of reference molecules, **SPDI** and **NPDI**, exhibit the characteristic spectral features of a singlet excited-state (S_1 to S_n transition) of a **PDI** chromophore in the initial time, which decays with the evolution of a triplet state of the monomeric unit with a weak spectral signature (Fig. S23 and S24†).[24,35,57,85,86]

Upon photoexcitation of **SC-SPDI$_2$** in TOL at 470 nm, fsTA spectra exhibit a strong negative ground state bleach (GSB) and weak stimulated emission (SE) between 450 and 563 nm, and excited-state absorption (ESA) maxima at 657 nm in the initial few picoseconds, assigned to the singlet excited state of **SC-SPDI$_2$** (^{1*}**SC-SPDI$_2$**, Fig. 4 and S25†). The rapid broadening of the ESA features between 570 and 760 nm and the evolution of a small negative SE signal in the 538–578 nm region within several hundred picoseconds are indicative of the structural relaxation to the unrelaxed excimer state (Ex*; *vide infra*). The SE signal maximum centered at 558 nm is comparable with the steady-state emission maximum ($\lambda_{max}^{Em} = 558$ nm), suggesting the emissive nature of the corresponding component. Later, singlet ESA disappears with the rise of a new broad and structureless ESA feature between 530 and 760 nm with an isosbestic point at ~601 nm, representing the relaxed excimer state (Ex). The presence of two excimer states arises from the structural rearrangement of the initially formed high-energy unrelaxed excimer state (Ex*) to a stable excimer state.[25,36,82] Global fitting of the fsTA data shows that the singlet excited-state/FE (A) decays to an unrelaxed excimer state (B) with a time constant of $\tau_{A\rightarrow B} = 11.3 \pm 0.1$ ps, followed by the rise of a structurally relaxed excimer state (C) occurring with a time constant of $\tau_{B\rightarrow C} = 1.12 \pm 0.02$ ns. Furthermore, the long-lived relaxed excimer state (C) does not decay completely within the experimental time window which is fitted with a time constant of 8.10 ± 0.01 ns.

Similarly, the fsTA spectra of **SC-NPDI$_2$** in TOL (Fig. S26 and S27†) display singlet excited or FE state features in early times (GSB/SE at 450–560 nm and ESA maxima at 620 nm), which decays to an intermediate unrelaxed excimer state ($\tau_{A\rightarrow B} = 23.6 \pm 0.2$ ps) characterized by the formation of a new SE band centered at 583 nm ($\lambda_{max}^{Em} = 584$ nm) and broadening of ESA spectral features in the 620–760 nm region (the isosbestic point at ~580 nm). Furthermore, the unrelaxed high-energy excimer (B) relaxes to form a stable, relaxed excimer state (C, $\tau_{B\rightarrow C} = 0.79 \pm 0.02$ ns) characterized by featureless and broad ESA, which does not decay within the experimental time window and

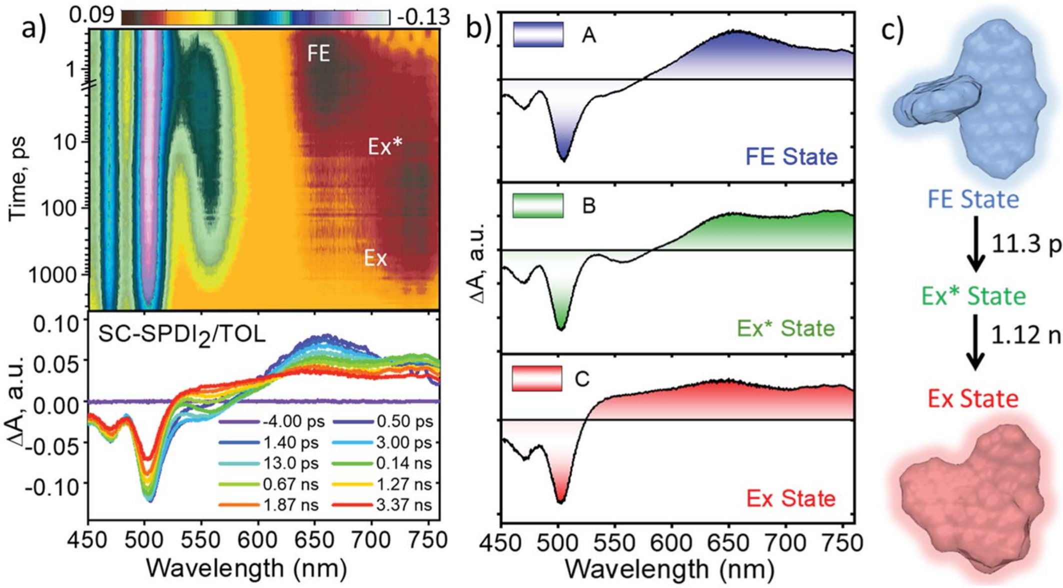

Fig. 4 (a) Femtosecond transient absorption contour maps (top) and spectra (bottom) of SC-SPDI$_2$ in toluene (TOL) showing the excited-state dynamics after photoexcitation at 470 nm. (b) Evolution associated difference spectra reconstructed from global analysis of the A → B → C → D model, where FE is the Frenkel exciton/singlet excited state; Ex* is the unrelaxed excimer state; Ex is the relaxed excimer state. (c) Schematic representation of excited-state dynamics of SC-SPDI$_2$ in toluene at room temperature.

is fitted with a time constant of 7.87 ± 0.02 ns. The two different excimer decay time constants agree with the fluorescence lifetime of **SC-SPDI$_2$** and **SC-NPDI$_2$** in TOL, indicating the emissive nature of the components B and C (Tables S6† and 1). The evolution of the new SE band maximum of **SC-SPDI$_2$** and **SC-NPDI$_2$** matches the steady-state emission maximum observed in TOL (Fig. S28†). The difference in the ESA signature of unrelaxed (B) and relaxed excimer (C) states is due to the higher photoluminescence behavior of the unrelaxed excimer state (Ex*) as compared to the stable excimer state (Ex). The approximate two-fold increase in the time constant for structural relaxation of **SC-SPDI$_2$** compared to **SC-NPDI$_2$** in TOL could have resulted from the difference in the excited-state energy landscapes.

In polar solvents (ACE and ACN), **SC-SPDI$_2$** shows GSB between 450 and 538 nm and ESA maxima at ∼662 nm in the initial time delays (Fig. 5, S29–S31† and Table 2). Subsequently, the synchronized evolution of the two transient species is characterized by positive ESA features in the visible region at ∼575 and 669 nm. The newly evolving ESA signature is attributed to the radical cation (ESA ∼ 575 nm) and radical anion (EAS ∼ 669 nm) of **SC-SPDI$_2$**, *i.e.*, the SB-CS state (Fig. S32–S34†). The concurrent growth of radical pairs of chromophores is the characteristic signature of intramolecular charge separation occurring between identical chromophores due to the solvent or structural vibration-induced symmetry breaking.[7,65,87,88] Furthermore, the radical pair of **SC-SPDI$_2$** decays to form a new transient state with broad spectral signatures resembling the characteristic excimer state features.[35,62,89] The sequential fitting of the fsTA data shows the ultrafast decay of the singlet excited state/Frenkel exciton (A) of **SC-SPDI$_2$** with the evolution of the SB-CS state (B) with a time constant of 1.5 ± 0.1 ps and 0.9 ± 0.1 ps in ACE and ACN, respectively, which is ∼8–13 fold faster than excimer formation in TOL. Afterward, the SB-CS state (B) decays to the relaxed excimer (C) with a time constant of approximately 2.01 ± 0.05 ns in ACE and 0.84 ± 0.02 ns in ACN (Table 2). The long-lived excimer state (C) is fitted with a time constant of 5.89 ± 0.01 ns in ACE and 5.81 ± 0.03 ns in ACN, assuming that photoluminescence of **SC-SPDI$_2$** in ACE (τ_{Fl}=5.89 ns) and ACN (τ_{Fl}=5.81 ns) originated from the relaxed excimer state (Ex).

The excited-state dynamics of **SC-NPDI$_2$** in ACE and ACN are similar to those of **SC-SPDI$_2$** in ACE and ACN, as shown in Fig. S35–S37.† The fsTA spectra at 0.5 ps show singlet excited-state/Frenkel exciton (A) features of **SC-NPDI$_2$** (ESA = 555−760 nm/GSB = <555 nm), which decays to the SB-CS state (B, $\tau_{\mathrm{A}\rightarrow\mathrm{B}}$ = 2.7 ± 0.02 ps for ACE and 1.4 ± 0.01 ps for ACN). The ESA bands centered at ∼561 nm (radical cation of **SC-NPDI$_2$**) and 673 nm (radical anion of **SC-NPDI$_2$**) appear in the initial few picoseconds, indicating the ultrafast SB-CS state formation (Fig. S35†).[24,57] Later, the SB-CS state (B) decays with the formation of a new excimer state (C) having a charge-transfer character ($\tau_{\mathrm{B}\rightarrow\mathrm{C}}$ = 1.66 ± 0.02 ns for ACE and 0.71 ± 0.02 ns for ACN). Energy level diagrams showing the solvent-dependent distinct excited-state decay processes occurring in **SC-SPDI$_2$** and **SC-NPDI$_2$** along with the geometries of the dimers in the ground state and relaxed excited-state are shown in Fig. 6. The excimer state of **SC-SPDI$_2$** and **SC-NPDI$_2$** in polar solvents resembles a SB-CS state with spectral broadening. As observed by Kim, Würthner and coworkers in bay-substituted perylenediimide cyclophane, this broad spectral feature can be assigned to an excimer state with a charge-transfer (CT) resonance character.[62] The lifetime of the long-lived CT resonance excimer state of **SC-SPDI$_2$** in ACE and ACN is fitted with ($\tau_{\mathrm{C}\rightarrow\mathrm{D}}$ = 3.82 ± 0.04 ns in ACE and 2.3 ± 0.04 ns in ACN) the observed fluorescence

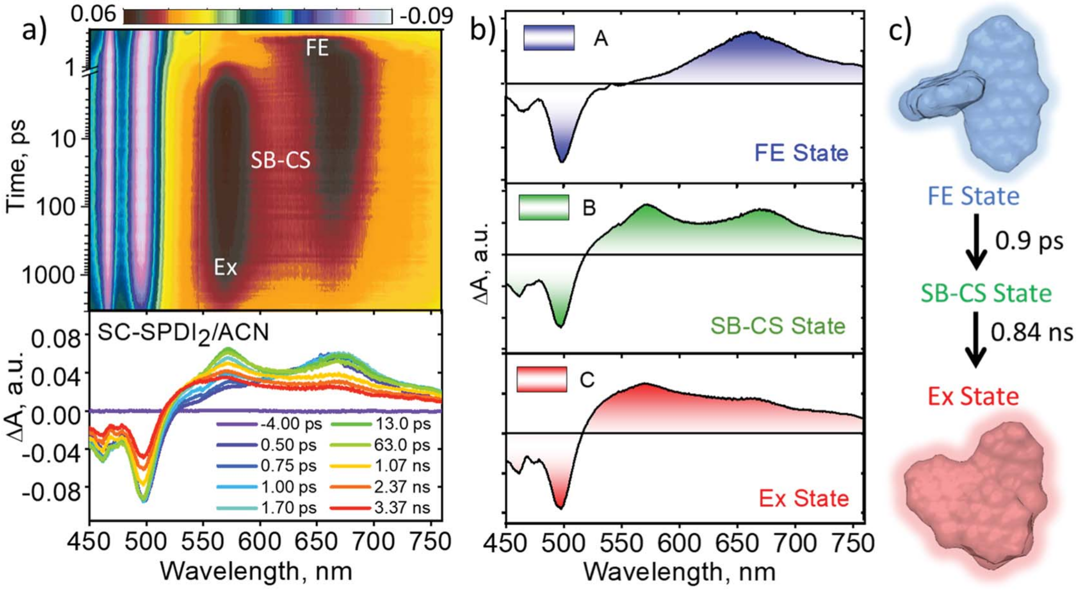

Fig. 5 (a) Femtosecond transient absorption contour maps (top) and spectra (bottom) of SC-SPDI$_2$ in acetonitrile (ACN) showing the excited-state dynamics after photoexcitation at 470 nm. (b) Evolution associated difference spectra reconstructed from global analysis of the A → B → C → D model, where FE is the Frenkel exciton/singlet excited state; SB-CS is the symmetry-breaking charge-separated state; Ex is the excimer state. (c) Schematic representative excited-state dynamics of SC-SPDI$_2$ in acetonitrile at room temperature.

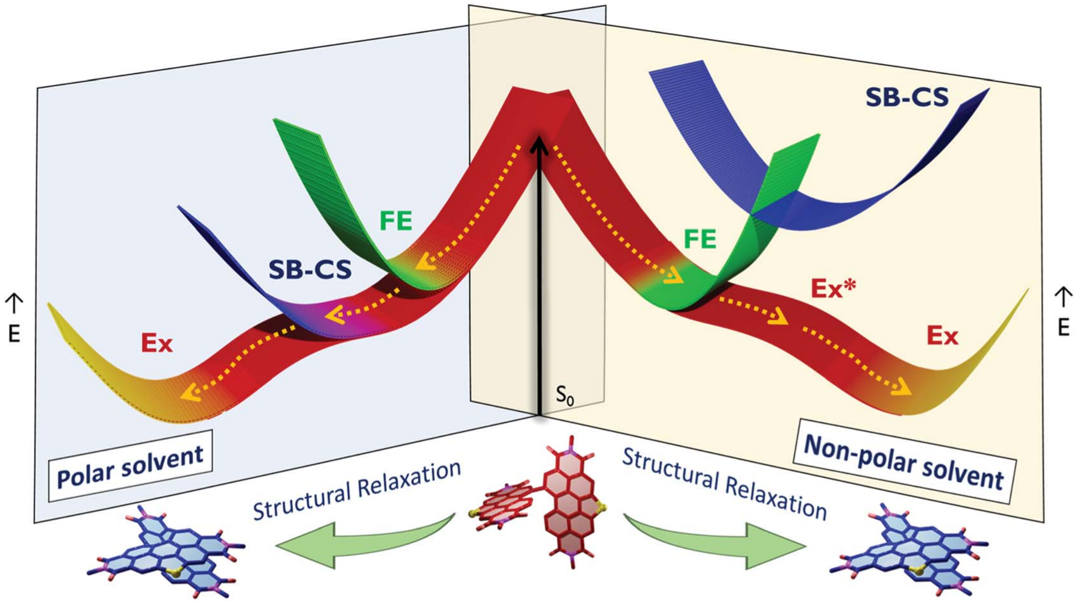

Fig. 6 The potential energy diagram summarizes the excited-state dynamics of SC-SPDI$_2$ and SC-NPDI$_2$ undergoing structural relaxation in polar solvents (ACE and ACN) and non-polar solvent (TOL), where FE is the Frenkel exciton, Ex* is the unrelaxed excimer state, Ex is the stable excimer state and SB-CS is the symmetry-breaking charge-separated state. The *x*-axis represents the reaction coordinate and E on the *y*-axis indicates the potential energy.

lifetime (Table 1). The decrease in the ratio of 0–0 and 0–1 vibronic band intensities in the GSB may be an indication of excited-state structural relaxation of **SC-SPDI$_2$** and **SC-NPDI$_2$** dimers from near-orthogonal arrangement to a relaxed foldamer structure (Fig. S38†).[36] Ultrafast spectroscopic techniques including time-resolved impulsive stimulated Raman spectroscopy (TR-ISRS), time-resolved IR spectroscopy (TR-IR) and femtosecond stimulated Raman spectroscopy (FSRS) have been previously employed to elucidate the structural dynamics of excimer evolution.[90–93]

To obtain further evidence on the late events of **SC-SPDI$_2$** and **SC-NPDI$_2$**, nanosecond transient absorption (nsTA) spectroscopy measurements were performed in different solvents (Fig. S39–S42†). In TOL, nsTA spectra of **SC-SPDI$_2$** show a positive ESA band at around 550 nm corresponding to the $T_1 \rightarrow T_n$ transition and negative GSB below 515 nm, which decay with a lifetime of 6.62 ± 0.02 μs. At the same time, **SC-NPDI$_2$** in TOL does not show any spectral signature of the triplet state, which might be a consequence of the low spin–orbit-induced intersystem crossing (SO-ISC).[94] Conversely, **SC-SPDI$_2$** and **SC-NPDI$_2$** in polar solvents (ACE and ACN) show the characteristic of a triplet manifold (GSB/ESA = 515 nm/550 nm for **SC-SPDI$_2$** and GSB/ESA = 535 nm/585 nm for **SC-NPDI$_2$**), which decay to the ground state with a lifetime of 3.15 ± 0.02 μs and 3.16 ± 0.03 μs for **SC-SPDI$_2$** and 2.21 ± 0.01 μs and 2.18 ± 0.02 μs for **SC-NPDI$_2$**, respectively. The overall excited state dynamics of **SC-SPDI$_2$** and **SC-NPDI$_2$** in different solvents are shown in Fig. S43–S46.† The population of excimer states through two competing pathways as a result of the varied interchromophoric coupling was reported by Wasielewski and co-workers in a cofacially arranged perylene dimer.[25] Due to cofacial arrangement, the perylene dimer exhibits partial excimer formation through an SB-CS intermediate state and direct excimer population (major pathway) in polar solvents. In the present case, effective electronic coupling between the FE state and SB-CS state in the near-orthogonal FC geometry of **SC-SPDI$_2$** and **SC-NPDI$_2$** facilitates the ultrafast SB-CS and suppresses the excimer formation in the initial time. This is further supported by the rate constant of SB-CS in polar solvents being 8–17 fold greater than the rate constant of Ex* formation or excited state structural relaxation in toluene (Table S10†). However, when the chromophores rearrange into a foldamer conformation, the initially populated SB-CS dissociates to the excimer state.

Excited-state fragment-based analysis

The nature of different excited-states of **SC-SPDI$_2$** and **SC-NPDI$_2$**, in their Franck–Condon (FC) near-orthogonal geometry and relaxed excited-state foldamer geometry, were evaluated by fragment-based excited-state analysis (Fig. 7, ESI, Section 1.7†).[95,96] The participation ratio (PR) defines the extent of delocalization of the excitation energy in different fragments (each annulated PDI monomer unit of dimers is considered as a fragment) and its magnitude will range from 2 (delocalized on 2 fragments) to 1 (localized on one fragment). The charge-transfer (CT) value describes the nature of the molecule's different excited-states. The CT value can vary from 1 to 0, where the excited-state having CT < 0.2 indicates the Frenkel exciton (FE) state and CT > 0.8 describes the charge-transfer state. Finally, the excited-state defined by CT values ranging from 0.2 to 0.8 (0.2 < CT < 0.8, PR > 1.25) is assigned to an excimer state.[95,97] In the FC geometry, **SC-SPDI$_2$** and **SC-NPDI$_2$** have four delocalized Frenkel exciton (FE) states, S$_1$, S$_2$, S$_3$, and S$_4$ (CT ≅

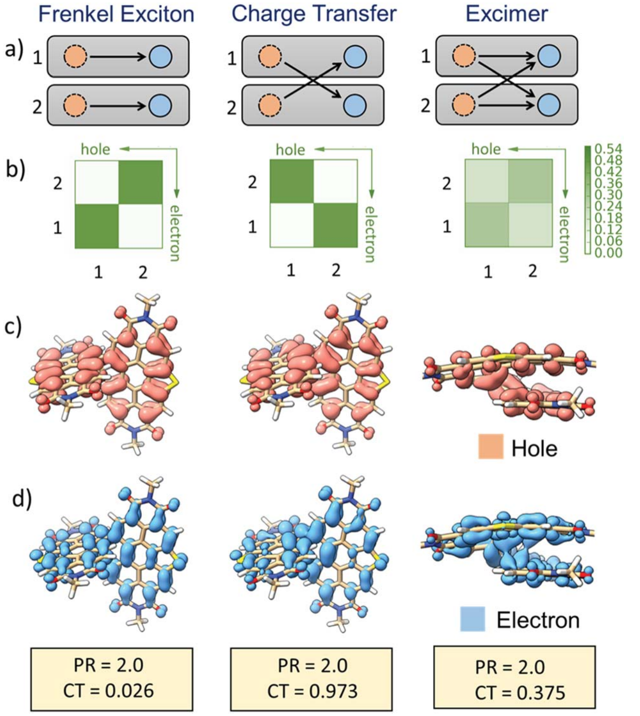

Fig. 7 Pictorial representation of the delocalized Frenkel exciton (left), charge resonance states (middle) of FC geometry, and the excimer state (right) of the relaxed foldamer structure of SC-SPDI$_2$. (a) Schematic representation of hole–electron distribution in the dimer, the rectangular box represents each fragment, dashed orange circles depict holes, and solid blue circles depict excited electrons. Hole–electron correlation plots (b) and the corresponding isosurface of the hole (c, orange) and electron (d, blue) distribution of different excited-states of SC-SPDI$_2$. The CT and PR values are given at the bottom to define the nature of excitations.

0 and PR = 2) and two near-degenerate charge-transfer/resonance states, S_5 and S_6 (CT ≅ 0.94 and PR = 2, Fig. S47–S49,† Tables S7 and S8†). The charge resonance states (S_5 and S_6, CT ≈ 1) and delocalized Frenkel exciton states (S_1–S_4, CT ≈ 0) are energetically well-separated in the FC geometry.

Fascinatingly, configuration mixing between the Frenkel exciton state and charge-resonance state occurs when the FC geometry (near-orthogonal arrangement) of **SC-SPDI$_2$** and **SC-NPDI$_2$** is transformed into an excited-state equilibrium geometry (π-stacked foldamer arrangement). The CT value of the first singlet excited-state (S_1) of the relaxed foldamer geometry shows a magnitude of 0.37 for **SC-SPDI$_2$** and 0.39 for **SC-NPDI$_2$**, along with a PR value of 2, indicating that the monomer units interact strongly to form the stabilized excimer state.[98] *i.e.*, the S_1 state of **SC-SPDI$_2$** and **SC-NPDI$_2$** in the foldamer arrangement does not remain as a pure Frenkel exciton but instead gains a partial CT character. The description is schematically and pictorially represented in Fig. 7 and S47† using electron–hole correlation plots and isosurfaces of **SC-SPDI$_2$** and **SC-NPDI$_2$**. The different excited states of **SC-SPDI$_2$** and **SC-NPDI$_2$** in the foldamer configuration are given in Tables S9 and S10† and Fig. S50 and S51.† In the case of the delocalized Frenkel exciton, both electron–hole (hole) and excited-electron densities are localized on the same molecular fragment and these local excitations on monomeric units get coupled to form a delocalized state (Fig. 7, left side). In the charge resonance state, the electron–hole and excited-electron densities are completely localized on different monomeric units and a linear combination of two charge-transfer transitions opposing each other with no net charge transfer is observed (Fig. 7, middle). Finally, the excimer state implies that electron–hole and excited-electron densities are delocalized over two monomeric units. *i.e.*, both the electron–hole and excited-electron of a monomeric unit can be found in the same or different monomeric units (Fig. 7, right side).[95–97]

Interplay of FE and CT contribution to the excimer state

The relative contributions of the FE and the CT states to an excimer state depend on the distance and relative orientation between the chromophore and dielectric medium around the chromophore.[4,97,99,100] In a non-polar solvent, TOL, the energy of the CS/CT state of **SC-SPDI$_2$** and **SC-NPDI$_2$** is higher than that of the singlet state/FE state; as a result, efficient mixing of the FE state with CT/CS is less probable. Consequently, the excimer having a more prominent FE character than CT character is observed in the fsTA spectra of **SC-SPDI$_2$** and **SC-NPDI$_2$** in TOL, which could be the reason for high ϕ_{Fl} of dimers in TOL (Fig. 4 and S26†). However, the excimer state spectral signatures of **SC-SPDI$_2$** and **SC-NPDI$_2$** in polar solvents nearly resemble the SB-CS state, with the positions of the radical pair bands being the same with broader ESA. This observation can be rationalized by the fact that the energy of the CS state is more stabilized than the FE state in polar solvents, facilitating the efficient mixing of the FE and CS states in the relaxed excited-state foldamer structure. Charge-transfer contribution to the excimer state of **SC-NPDI$_2$** is higher than that of **SC-SPDI$_2$** in polar solvents, which could stem from the reduced centroid to centroid distance (d) between monomers in the excited-state foldamer structure and the reduced energy difference between the FE and the CS states of **SC-NPDI$_2$** compared to those of **SC-SPDI$_2$** (Fig. S4† and Table 2). Photoluminescence quenching and a decrease in the fluorescence lifetime of **SC-NPDI$_2$** as the dielectric medium changes from ACE to ACN is attributed to the enhanced charge-transfer (CT) resonance character of the emissive excimer state. Due to the weak CT resonance nature of the emissive excimer state in **SC-SPDI$_2$**, the photoluminescence quantum yield and fluorescence lifetimes are nearly unperturbed by a change in solvent polarity, *i.e.*, ACE to ACN (Table 1).

Conclusions

In conclusion, we report unequivocal evidence for the excited-state structural relaxation of **SC-SPDI$_2$** and **SC-NPDI$_2$** hampering the efficiency of the SB-CS state. Conjoint spectroscopic and theoretical investigations have rationalized the structural dynamics in the excited state and the manifestation of an excimer-like state in the π-stacked foldamer structure. The solvent polarity-dependent fsTA measurements of **SC-SPDI$_2$** and **SC-NPDI$_2$** reveal ultrafast SB-CS in polar solvents, in contrast to direct excimer formation observed in non-polar TOL. Molecular rearrangement of **SC-SPDI$_2$** and **SC-NPDI$_2$** in the excited-state transforms the initially populated SB-CS state into a CT resonance-enhanced excimer state, limiting the SB-CS state lifetime. These observations reinstate the importance of rigid molecular architectures, reminiscent of conformationally rigid special pairs of photosynthetic reaction centers embedded in protein scaffolds, exhibiting efficient SB-CS as non-fullerene acceptors in OPVs.

Data availability

All experimental/computational data and procedures are available in the ESI.†

Author contributions

E. S., J. S. and M. H. conceived the project; E. S and J. S. carried out the measurements. E. S., J. S. and M. H. analysed the results; E. S., J. S., and M. H. wrote the manuscript; M. H. supervised the research.

Conflicts of interest

There are no conflicts to declare.

Acknowledgements

M. H. acknowledges the Nanomission project (DST/NM/TUE/EE-01/2019) of the Department of Science and Technology (DST), Government of India, for financial support. E. S. acknowledges UGC for financial assistance. We thank Dr Sooraj Kunnikuruvan for fruitful discussions. We greatly acknowledge the support for high-performance computing time at the Padmanabha cluster, IISER Thiruvananthapuram, India.

References

1 M. R. Wasielewski, *Chem. Rev.*, 2002, **92**, 435–461.

2 E. Vauthey, *ChemPhysChem*, 2012, **13**, 2001–2011.

3 E. Sebastian and M. Hariharan, *ACS Energy Lett.*, 2022, **7**, 696–711.

4 R. M. Young and M. R. Wasielewski, *Acc. Chem. Res.*, 2020, **53**, 1957–1968.

5 H. Halperin, K. Dejong, R. E. W Adams, C. C. Coggins, N. Hammond, D. S. Gotufried, M. A. Steffen and S. G. Boxer, *Science*, 1991, **251**, 662–665.

6 B. Dereka, M. Koch and E. Vauthey, *Acc. Chem. Res.*, 2017, **50**, 426–434.

7 C. Lin, T. Kim, J. D. Schultz, R. M. Young and M. R. Wasielewski, *Nat. Chem.*, 2022, **7**, 786–793.

8 D. A. Cherepanov, I. V. Shelaev, F. E. Gostev, A. Petrova, A. V. Aybush, V. A. Nadtochenko, W. Xu, J. H. Golbeck and A. Y. Semenov, *J. Photochem. Photobiol., B*, 2021, **217**, 112154.

9 H. Tamura, K. Saito and H. Ishikita, *Proc. Natl. Acad. Sci. U. S. A.*, 2020, **117**, 16373–16382.

10 B. A. Diner and F. Rappaport, *Annu. Rev. Plant Biol.*, 2003, **53**, 551–580.

11 S. Vasil'ev, J. R. Shen, N. Kamiya and D. Bruce, *FEBS Lett.*, 2004, **561**, 111–116.

12 H. Tamura, K. Saito and H. Ishikita, *Chem. Sci.*, 2021, **12**, 8131–8140.

13 D. J. Lockhart and S. G. Boxer, *Biochemistry*, 2002, **26**, 664–668.

14 J. Hong, M. J. Sung, H. Cha, C. E. Park, J. R. Durrant, T. K. An, Y. H. Kim and S. K. Kwon, *ACS Appl. Mater. Interfaces*, 2018, **10**, 36037–36046.

15 J. L. Brédas, E. H. Sargent and G. D. Scholes, *Nat. Mater.*, 2016, **16**, 35–44.

16 V. Coropceanu, X. K. Chen, T. Wang, Z. Zheng and J. L. Brédas, *Nat. Rev. Mater.*, 2019, **4**, 689–707.

17 A. J. Gillett, A. Privitera, R. Dilmurat, A. Karki, D. Qian, A. Pershin, G. Londi, W. K. Myers, J. Lee, J. Yuan, S. J. Ko, M. K. Riede, F. Gao, G. C. Bazan, A. Rao, T. Q. Nguyen, D. Beljonne and R. H. Friend, *Nature*, 2021, **597**, 666–671.

18 M. Lv, X. Lu, Y. Jiang, M. E. Sandoval-Salinas, D. Casanova, H. Sun, Z. Sun, J. Xu, Y. Yang and J. Chen, *Angew. Chem., Int. Ed.*, 2022, **61**, e202113190.

19 S. M. Menke, N. A. Ran, G. C. Bazan and R. H. Friend, *Joule*, 2018, **2**, 25–35.

20 J. Benduhn, K. Tvingstedt, F. Piersimoni, S. Ullbrich, Y. Fan, M. Tropiano, K. A. McGarry, O. Zeika, M. K. Riede, C. J. Douglas, S. Barlow, S. R. Marder, D. Neher, D. Spoltore and K. Vandewal, *Nat. Energy*, 2017, **2**, 1–6.

21 A. N. Bartynski, M. Gruber, S. Das, S. Rangan, S. Mollinger, C. Trinh, S. E. Bradforth, K. Vandewal, A. Salleo, R. A. Bartynski, W. Bruetting and M. E. Thompson, *J. Am. Chem. Soc.*, 2015, **137**, 5397–5405.

22 N. Kaul and R. Lomoth, *J. Am. Chem. Soc.*, 2021, **143**, 10816–10821.

23 C. E. Ramirez, S. Chen, N. E. Powers-Riggs, I. Schlesinger, R. M. Young and M. R. Wasielewski, *J. Am. Chem. Soc.*, 2020, **142**, 18243–18250.

24 Y. Guo, Z. Ma, X. Niu, W. Zhang, M. Tao, Q. Guo, Z. Wang and A. Xia, *J. Am. Chem. Soc.*, 2019, **141**, 12789–12796.

25 R. E. Cook, B. T. Phelan, R. J. Kamire, M. B. Majewski, R. M. Young and M. R. Wasielewski, *J. Phys. Chem. A*, 2017, **121**, 1607–1615.

26 J. Sung, A. Nowak-Król, F. Schlosser, B. Fimmel, W. Kim, D. Kim and F. Würthner, *J. Am. Chem. Soc.*, 2016, **138**, 9029–9032.

27 P. Spenst, R. M. Young, M. R. Wasielewski and F. Würthner, *Chem. Sci.*, 2016, **7**, 5428–5434.

28 P. Roy, G. Bressan, J. Gretton, A. N. Cammidge and S. R. Meech, *Angew. Chem., Int. Ed.*, 2021, **60**, 10568–10572.

29 J. Kong, W. Zhang, G. Li, D. Huo, Y. Guo, X. Niu, Y. Wan, B. Tang and A. Xia, *J. Phys. Chem. Lett.*, 2020, **11**, 10329–10339.

30 A. Aster, G. Licari, F. Zinna, E. Brun, T. Kumpulainen, E. Tajkhorshid, J. Lacour and E. Vauthey, *Chem. Sci.*, 2019, **10**, 10629–10639.

31 Y. Wu, R. M. Young, M. Frasconi, S. T. Schneebeli, P. Spenst, D. M. Gardner, K. E. Brown, F. Würthner,

J. F. Stoddart and M. R. Wasielewski, *J. Am. Chem. Soc.*, 2015, **137**, 13236–13239.
32 E. Sebastian and M. Hariharan, *J. Am. Chem. Soc.*, 2021, **143**, 13769–13781.
33 J. M. Giaimo, A. V. Gusev and M. R. Wasielewski*, *J. Am. Chem. Soc.*, 2002, **124**, 8530–8531.
34 C. B. Dover, J. K. Gallaher, L. Frazer, P. C. Tapping, A. J. Petty, M. J. Crossley, J. E. Anthony, T. W. Kee and T. W. Schmidt, *Nat. Chem.*, 2018, **10**, 305–310.
35 E. A. Margulies, L. E. Shoer, S. W. Eaton and M. R. Wasielewski, *Phys. Chem. Chem. Phys.*, 2014, **16**, 23735–23742.
36 Y. J. Bae, D. Shimizu, J. D. Schultz, G. Kang, J. Zhou, G. C. Schatz, A. Osuka and M. R. Wasielewski, *J. Phys. Chem. A*, 2020, **124**, 8478–8487.
37 R. Singh, M. Kim, J. J. Lee, T. Ye, P. E. Keivanidis and K. Cho, *J. Mater. Chem. C*, 2020, **8**, 1686–1696.
38 R. Wang, C. Zhang, Q. Li, Z. Zhang, X. Wang and M. Xiao, *J. Am. Chem. Soc.*, 2020, **142**, 12751–12759.
39 J. Hoche, M. Flock, X. Miao, L. N. Philipp, M. Wenzel, I. Fischer and R. Mitric, *Chem. Sci.*, 2021, **12**, 11965–11975.
40 T. Yamakado, S. Takahashi, K. Watanabe, Y. Matsumoto, A. Osuka, S. Saito, T. Yamakado, S. Takahashi, K. W. Atanabe, Y. M. Atsumoto, P. R. A. Osuka and S. Saito, *Angew. Chem., Int. Ed.*, 2018, **57**, 5438–5443.
41 J. H. Golden, L. Estergreen, T. Porter, A. C. Tadle, D. M. R. Sylvinson, J. W. Facendola, C. P. Kubiak, S. E. Bradforth and M. E. Thompson, *ACS Appl. Energy Mater.*, 2018, **1**, 1083–1095.
42 M. Jurczok, P. Plaza, M. M. Martin, Y. H. Meyer and W. Rettig, *Chem. Phys.*, 2000, **253**, 339–349.
43 J. J. Piet, W. Schuddeboom, B. R. Wegewijs, F. C. Grozema and J. M. Warman, *J. Am. Chem. Soc.*, 2001, **123**, 5337–5347.
44 H. Song, H. Zhao, Y. Guo, A. M. Philip, Q. Guo, M. Hariharan and A. Xia, *J. Phys. Chem. C*, 2020, **124**, 237–245.
45 Z. Piontkowski and D. W. McCamant, *J. Am. Chem. Soc.*, 2018, **140**, 11046–11057.
46 L. Estergreen, A. R. Mencke, D. E. Cotton, N. V. Korovina, J. Michl, S. T. Roberts, M. E. Thompson and S. E. Bradforth, *Acc. Chem. Res.*, 2022, **55**, 1561–1572.
47 A. D. Hendsbee, J. P. Sun, W. K. Law, H. Yan, I. G. Hill, D. M. Spasyuk and G. C. Welch, *Chem. Mater.*, 2016, **28**, 7098–7109.
48 R. Xin, J. Feng, C. Zeng, W. Jiang, L. Zhang, D. Meng, Z. Ren, Z. Wang and S. Yan, *ACS Appl. Mater. Interfaces*, 2017, **9**, 2739–2746.
49 M. P. Lijina, A. Benny, R. Ramakrishnan, N. G. Nair and M. Hariharan, *J. Am. Chem. Soc.*, 2020, **142**, 17393–17402.
50 A. M. Philip, A. R. Mallia and M. Hariharan, *J. Phys. Chem. Lett.*, 2016, **7**, 4751–4756.
51 M. Madhu, R. Ramakrishnan, V. Vijay and M. Hariharan, *Chem. Rev.*, 2021, **121**, 8234–8284.
52 K. Nagarajan, A. R. Mallia, K. Muraleedharan and M. Hariharan, *Chem. Sci.*, 2017, **8**, 1776–1782.
53 A. Benny, R. Ramakrishnan and M. Hariharan, *Chem. Sci.*, 2021, **12**, 5064–5072.
54 D. Meng, D. Sun, C. Zhong, T. Liu, B. Fan, L. Huo, Y. Li, W. Jiang, H. Choi, T. Kim, J. Y. Kim, Y. Sun, Z. Wang and A. J. Heeger, *J. Am. Chem. Soc.*, 2016, **138**, 375–380.
55 D. Sun, D. Meng, Y. Cai, B. Fan, Y. Li, W. Jiang, L. Huo, Y. Sun and Z. Wang, *J. Am. Chem. Soc.*, 2015, **137**, 11156–11162.
56 H. Qian, W. Yue, Y. Zhen, S. Di Motta, E. Di Donato, F. Negri, J. Qu, W. Xu, D. Zhu and Z. Wang, *J. Org. Chem.*, 2009, **74**, 6275–6282.
57 I. K. Madu, H. Jiang, A. Laventure, P. M. Zimmerman, G. C. Welch and T. Goodson, *J. Phys. Chem. C*, 2021, **125**, 10500–10515.
58 E. Sebastian, A. M. Philip, A. Benny and M. Hariharan, *Angew. Chem., Int. Ed.*, 2018, **57**, 15696–15701.
59 C. Kaufmann, D. Bialas, M. Stolte and F. Würthner, *J. Am. Chem. Soc.*, 2018, **140**, 9986–9995.
60 B. S. Basel, C. Hetzer, J. Zirzlmeier, D. Thiel, R. Guldi, F. Hampel, A. Kahnt, T. Clark, D. M. Guldi and R. R. Tykwinski, *Chem. Sci.*, 2019, **10**, 3854–3863.
61 S. A. Bagnich, S. Athanasopoulos, A. Rudnick, P. Schroegel, I. Bauer, N. C. Greenham, P. Strohriegl and A. Köhler, *J. Phys. Chem. C*, 2015, **119**, 2380–2387.
62 W. Kim, A. Nowak-Król, Y. Hong, F. Schlosser, F. Würthner and D. Kim, *J. Phys. Chem. Lett.*, 2019, **10**, 1919–1927.
63 M. Nazari, E. Cieplechowicz, T. A. Welsh and G. C. Welch, *New J. Chem.*, 2019, **43**, 5187–5195.
64 R. J. Lindquist, K. M. Lefler, K. E. Brown, S. M. Dyar, E. A. Margulies, R. M. Young and M. R. Wasielewski, *J. Am. Chem. Soc.*, 2014, **136**, 14912–14923.
65 T. Kim, J. Kim, H. Mori, S. Park, M. Lim, A. Osuka and D. Kim, *Phys. Chem. Chem. Phys.*, 2017, **19**, 13970–13977.
66 R. F. Fink, J. Seibt, V. Engel, M. Renz, M. Kaupp, S. Lochbrunner, H. M. Zhao, J. Pfister, F. Würthner and B. Engels, *J. Am. Chem. Soc.*, 2008, **130**, 12858–12859.
67 J. Da Chai and M. Head-Gordon, *Phys. Chem. Chem. Phys.*, 2008, **10**, 6615–6620.
68 F. Weigend and R. Ahlrichs, *Phys. Chem. Chem. Phys.*, 2005, **7**, 3297–3305.
69 S. Grimme, J. Antony, S. Ehrlich and H. Krieg, *J. Chem. Phys.*, 2010, **132**, 154104.
70 A. B. Bornhof, A. Bauzá, A. Aster, M. Pupier, A. Frontera, E. Vauthey, N. Sakai and S. Matile, *J. Am. Chem. Soc.*, 2018, **140**, 4884–4892.
71 B. Fimmel, M. Son, Y. M. Sung, M. Grüne, B. Engels, D. Kim and F. Würthner, *Chem. - Eur. J.*, 2015, **21**, 615–630.
72 J. Chen, A. W. Ziegler, B. Zhao, W. Wan and A. D. Q. Li, *Chem. Commun.*, 2017, **53**, 4993–4996.
73 Y. Hong, J. Kim, W. Kim, C. Kaufmann, H. Kim, F. Würthner and D. Kim, *J. Am. Chem. Soc.*, 2020, **142**, 7845–7857.
74 E. P. Farr, M. T. Fontana, C. C. Zho, P. Wu, Y. L. Li, N. Knutson, Y. Rubin and B. J. Schwartz, *J. Phys. Chem. C*, 2019, **123**, 2127–2138.
75 H. Yongseok, W. Kim, T. Kim, C. Kaufmann, H. Kim, F. Würthner and D. Kim, *Angew. Chem., Int. Ed.*, 2021, e202114474.

76 H. Osaki, C.-M. Chou, M. Taki, K. Welke, D. Yokogawa, S. Irle, Y. Sato, T. Higashiyama, S. Saito, A. Fukazawa and S. Yamaguchi, *Angew. Chem., Int. Ed.*, 2016, **128**, 7247–7251.

77 D. Veldman, S. M. A. Chopin, S. C. J. Meskers, M. M. Groeneveld, R. M. Williams and R. A. J. Janssen, *J. Phys. Chem. A*, 2008, **112**, 5846–5857.

78 F. C. Spano and H. Yamagata, *J. Phys. Chem. B*, 2010, **115**, 5133–5143.

79 L. Van Dijk, P. A. Bobbert and F. C. Spano, *J. Phys. Chem. B*, 2009, **113**, 9708–9717.

80 F. C. Spano and C. Silva, *Annu. Rev. Phys. Chem.*, 2014, **65**, 477–500.

81 J. H. Golden, L. Estergreen, T. Porter, A. C. Tadle, D. M. R. Sylvinson, J. W. Facendola, C. P. Kubiak, S. E. Bradforth and M. E. Thompson, *ACS Appl. Energy Mater.*, 2018, **1**, 1083–1095.

82 Y. Hong, J. Kim, W. Kim, C. Kaufmann, H. Kim, F. Würthner and D. Kim, *J. Am. Chem. Soc.*, 2020, **142**, 7845–7857.

83 A. Weller, *Z. Phys. Chem.*, 1982, **133**, 93–98.

84 H. Imahori, K. Hagiwara, M. Aoki, T. Akiyama, S. Taniguchi, T. Okada, M. Shirakawa and Y. Sakata, *J. Am. Chem. Soc.*, 1996, **118**, 11771–11782.

85 A. Mohan, E. Sebastian, M. Gudem and M. Hariharan, *J. Phys. Chem. B*, 2020, **124**, 6867–6874.

86 I. Solymosi, S. Krishna, E. Nuin, H. Maid, B. Scholz, D. M. Guldi, M. E. Pérez-Ojeda and A. Hirsch, *Chem. Sci.*, 2021, **12**, 15491–15502.

87 V. Markovic, D. Villamaina, I. Barabanov, L. M. Lawson Daku and E. Vauthey, *Angew. Chem., Int. Ed.*, 2011, **50**, 7596–7598.

88 S. Amthor, C. Lambert, S. Dümmler, I. Fischer and J. Schelter, *J. Phys. Chem. A*, 2006, **110**, 5204–5214.

89 K. E. Brown, W. A. Salamant, L. E. Shoer, R. M. Young and M. R. Wasielewski, *J. Phys. Chem. Lett.*, 2014, **5**, 2588–2593.

90 Y. Wu, J. Zhou, B. T. Phelan, C. M. Mauck, J. F. Stoddart, R. M. Young and M. R. Wasielewski, *J. Am. Chem. Soc.*, 2017, **139**, 14265–14276.

91 C. M. Mauck, R. M. Young and M. R. Wasielewski, *J. Phys. Chem. A*, 2017, **121**, 784–792.

92 W. Kim, T. Kim, S. Kang, Y. Hong, F. Würthner and D. Kim, *Angew. Chem., Int. Ed.*, 2020, **59**, 8571–8578.

93 E. R. Kennehan, C. Grieco, A. N. Brigeman, G. S. Doucette, A. Rimshaw, K. Bisgaier, N. C. Giebink and J. B. Asbury, *Phys. Chem. Chem. Phys.*, 2017, **19**, 24829–24839.

94 K. M. Lefler, K. E. Brown, W. A. Salamant, S. M. Dyar, K. E. Knowles and M. R. Wasielewski, *J. Phys. Chem. A*, 2013, **117**, 10333–10345.

95 F. Plasser and H. Lischka, *J. Chem. Theory Comput.*, 2012, **8**, 2777–2789.

96 F. Plasser, *J. Chem. Phys.*, 2020, **152**, 084108.

97 L. M. Ibele, P. A. Sánchez-Murcia, S. Mai, J. J. Nogueira and L. González, *J. Phys. Chem. Lett.*, 2020, **11**, 7483–7488.

98 A. L. L. East and E. C. Lim, *J. Chem. Phys.*, 2000, **113**, 8981.

99 J. Sung, A. Nowak-Król, F. Schlosser, B. Fimmel, W. Kim, D. Kim and F. Würthner, *J. Am. Chem. Soc.*, 2016, **138**, 9029–9032.

100 D. Casanova, *Int. J. Quantum Chem.*, 2015, **115**, 442–452.